J Low Temp Phys (2016) 184:634–641
DOI 10.1007/s10909-016-1576-y

Advanced ACTPol Multichroic Polarimeter Array Fabrication Process for 150 mm Wafers

S. M. Duff[1] · J. Austermann[1] · J. A. Beall[1] · D. Becker[1] · R. Datta[2] · P. A. Gallardo[3] · S. W. Henderson[3] · G. C. Hilton[1] · S. P. Ho[4] · J. Hubmayr[1] · B. J. Koopman[3] · D. Li[5] · J. McMahon[2] · F. Nati[6] · M. D. Niemack[3] · C. G. Pappas[4] · M. Salatino[4] · B. L. Schmitt[6] · S. M. Simon[4] · S. T. Staggs[4] · J. R. Stevens[3] · J. Van Lanen[1] · E. M. Vavagiakis[3] · J. T. Ward[6] · E. J. Wollack[7]

Received: 30 September 2015 / Accepted: 2 March 2016 / Published online: 22 March 2016

Abstract Advanced ACTPol (AdvACT) is a third-generation cosmic microwave background receiver to be deployed in 2016 on the Atacama Cosmology Telescope (ACT). Spanning five frequency bands from 25 to 280 GHz and having just over 5600 transition-edge sensor (TES) bolometers, this receiver will exhibit increased sensitivity and mapping speed compared to previously fielded ACT instruments. This paper presents the fabrication processes developed by NIST to scale to large arrays of feedhorn-coupled multichroic AlMn-based TES polarimeters on 150-mm diameter wafers. In addition to describing the streamlined fabrication process which enables high yields of densely packed detectors across larger wafers, we report the details of process improvements for sensor (AlMn) and insulator (SiN_x) materials and microwave structures, and the resulting performance improvements.

Keywords AlMn · Multichroic · Polarimeter · SiN_x · Transition-edge sensor

✉ S. M. Duff
shannon.duff@nist.gov

1 National Institute of Standards and Technology, 325 Broadway, Boulder, CO 80305, USA

2 Department of Physics, University of Michigan, Ann Arbor, MI 48103, USA

3 Department of Physics, Cornell University, Ithaca, NY 14853, USA

4 Department of Astrophysical Sciences, Princeton University, Princeton, NJ 08544, USA

5 SLAC National Accelerator Laboratory, 2575 Sandy Hill Road, Menlo Park, CA 94025, USA

6 Department of Physics and Astronomy, University of Pennsylvania, Philadelphia, PA 19104, USA

7 NASA Goddard Space Flight Center, Greenbelt, MD 20771, USA

1 Introduction

Study of the cosmic microwave background (CMB) provides a remarkable probe of cosmology. Its polarization may contain the signature of an inflationary epoch in its B-modes [1] and reveal the masses of the neutrinos [2]. B-mode detections have been reported over a broad range of angular scales [3–6]. These observations validate the experimental approach; however, accessing the tantalizing new physics and cosmology will require instruments with greater mapping speed and increased frequency coverage. To this end, we are developing monolithic, 150-mm diameter polarimeter arrays, in which each spatial pixel senses linear polarization over more than an octave of bandwidth, which is partitioned into two frequency sub-bands.

Multichroic, horn-coupled polarimeters at 90/150 GHz and 230/350 GHz have previously been reported [7,8], and an array of 90/150 GHz detectors, fabricated from 76.2-mm diameter wafers has been deployed in ACTPol [9,10]. In this paper we present the 150 mm wafer scale fabrication process of 150/230 GHz multichroic, feedhorn-coupled polarimeter arrays, detailing several aspects of the design and process flow which have been streamlined to ensure high yield over the larger wafer area. Included are a reduction in the number of fabrication steps, the use of new materials for sensors and insulators, and pixel-to-bond-pad wiring defined by stepped lithography. We demonstrate this approach with 150/230 GHz single pixels, which exhibit good optical coupling and frequency diplexing. Arrays of this architecture are scheduled for deployment in Advanced ACTPol (AdvACT) [11].

2 Multichroic Feedhorn-Coupled Polarimeters

The AdvACT detectors build upon the feedhorn-coupled multichroic 90/150 GHz polarimeter architecture developed for ACTPol, described by McMahon et al. [12]. We have optimized the high-frequency detector design for this third-generation receiver for the 150/230 GHz bands. As described in Sect. 3, the dielectric material has been switched to SiN_x from SiO_x and the transition-edge sensor (TES) material to an AlMn-alloy from a MoCu bilayer.

Each pixel (Fig. 1) consists of four TESs, allowing for individual measurements of the 150 and 230 GHz frequency bands, each in two orthogonal polarizations. The signal captured by the silicon platelet feedhorn is radiatively coupled to Nb transmission lines via the planar orthomode transducer (OMT), where it is split into x- and y-polarizations. In-line stub filters define the two passbands prior to the signals being routed to a hybrid tee, which produces a sum and a difference output from two input signals. The higher order modes from the sum output are terminated on the substrate and the lowest order TE_{11} mode from the difference output is routed to a bolometer for detection. Each AlMn TES is on a thermally isolated silicon nitride membrane suspended by four narrow legs and measures a change in temperature as the TE_{11} signal is dissipated through lossy gold meander structures in the sensor. A 500-nm-thick PdAu layer is deposited on each TES island to add heat capacity and stabilize the detector against electrothermal oscillation.

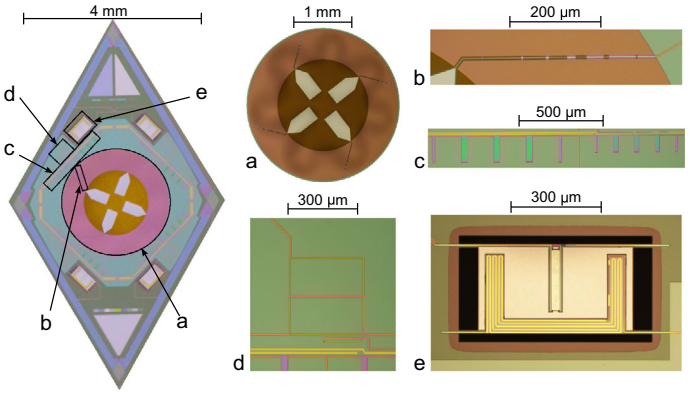

Fig. 1 *Left* Optical microscope image of one high-frequency 150/230 GHz multichroic single pixel. *Right* Zoomed images of the major pixel components: **a** the planar orthomode transducer, **b** the microstrip to coplanar waveguide transmission line, **c** the in-line stub filters, **d** the 180° hybrid tee, and **e** one of the AlMn TESs, which is thermally isolated on a SiN_x membrane suspended with four narrow legs (Color figure online)

3 Streamlined Fabrication Process

The fabrication process for the AdvACT detector arrays, developed at NIST, uses 150 mm silicon (100) wafers coated with 450 nm of thermally grown SiO_x and 2 µm of low-pressure chemical vapor deposited (LPCVD) low-stress SiN_x. The SiN_x supports the TES membranes and the SiO_x acts as the etch stop for the deep reactive ion etch (DRIE) step. Two subsequent plasma-enhanced chemical vapor deposition (PECVD) SiN_x layers constitute the (1) Nb transmission line dielectric and (2) passivation. A cross-sectional diagram of a TES is shown in Fig. 2.

3.1 Scaling to 150 mm

Previous generations of polarization-sensitive ACT detector arrays have been fabricated on 76.2-mm diameter silicon wafers. Scaling to 150-mm diameter silicon wafers requires a more robust and streamlined fabrication process with improved uniformity. In addition to decreasing the total wafer count for a single ACT focal plane from five 76.2 mm wafers to one 150 mm wafer, we have also decreased the total number of unit steps in the fabrication process by approximately 25 %, compared to the previous generation of ACTPol detector arrays.

By using rhombus-shaped pixels and wiring tracks designed as repeating units (Fig. 2), we are able to pattern every frontside layer with stepped lithography in a close-packed arrangement. This is preferential to contact lithography for patterning closely spaced wiring layers, which is prone to defects and, therefore, decreased detector yield. Furthermore, by arraying the rhombus-shaped pixels into three identical meta-rhombus sections, we fill the 150 mm wafer with an easy-to-repeat pattern. We have also implemented a partially automated layout parameter-driven code, which

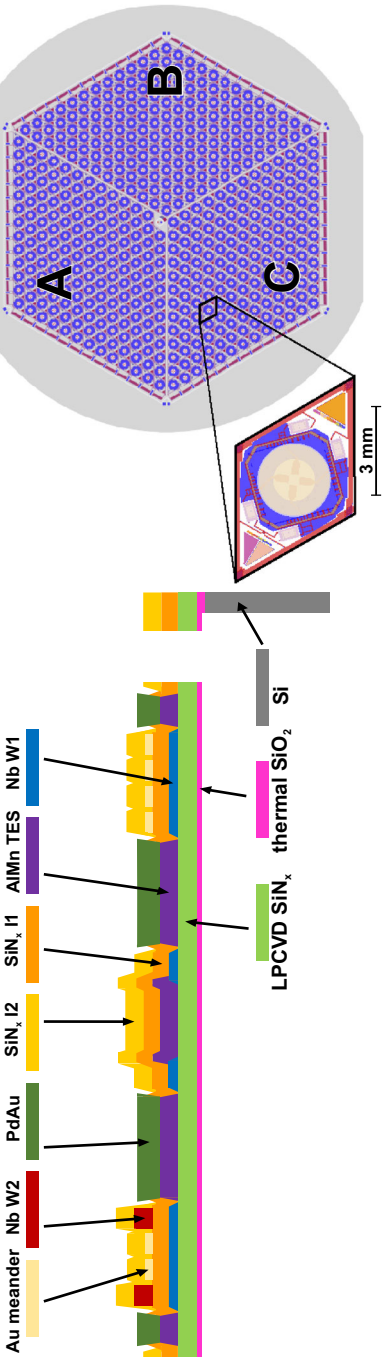

Fig. 2 *Left* Cross-section view of an AlMn-alloy TES showing each layer of the fabrication process. (1) coat 150 mm Si (100) wafers with thermal SiO_x and LPCVD low-stress SiN_x; (2) DC sputter deposition, patterning, and SF_6-based etch of Nb (W1) ground plane and wiring layer; (3) DC sputter deposition, patterning, and wet etch of AlMn TES with Transene Type A etchant heated to ~45 °C; (4) anneal AlMn to set T_c; (5) PECVD deposition, patterning, and CF_4-based etch of SiN_x (I1) dielectric layer for transmission lines; (6) DC sputter deposition, patterning, and SF_6-based etch of second Nb (W2) wiring layer; (7) patterning, evaporation, and liftoff of Ti/Au for meander structures; (8) PECVD deposition, patterning, and CF_4-based etch of second SiN_x dielectric layer for passivation; (9) patterning and CF_4-based etch of remaining dielectric from TES; (10) patterning, DC sputter deposition, and liftoff of PdAu for extra heat capacity; (11) patterning and CF_4-based etch of frontside SiN_x and SiO_x to define TES leg width; (12) CF_4-based etch of backside SiN_x and SiO_x; and (13) patterning and SF_6-based deep etch of backside Si to define membranes. *Right* A CAD rendering of 150/230 GHz multichroic polarimeter array for AdvACT having a total of 2012 TESs is shown overlayed on a 150-mm diameter wafer. Utilizing 100 % stepped lithography allows for tightly packed rhombus-shaped pixels, small wiring widths and pitches, and low wiring layer defects. Three identical meta-rhombus sections (**A**–**C**) are implemented with rotation to eliminate multiple sets of reticles (Color figure online)

allows straightforward modification of pixel size, wiring width and pitch, and bond-pad placement.

3.2 AlMn Transition-Edge Sensors

Superconducting TESs require superconducting films with critical temperatures (T_c) and other properties that can be tailored to the particular requirements of individual applications. We have developed AlMn films with a tunable T_c [13–15]. The addition of Mn to Al suppresses T_c, but does not significantly broaden the superconducting density of states of the Al. By choosing the appropriate concentration of Mn dopant in Al, we have demonstrated repeatable and uniform T_c on a 150 mm wafer.

Replacement of the MoCu bilayer used in ACTPol with an AlMn-alloy TES material not only avoids challenges associated with MoCu [16], but also results in a more flexible and streamlined process. For the AdvACT targeted T_c of 160 mK, the required thickness of the Mo film, which sets T_c for this bilayer system, would be thin (65 nm), making reproducibility a challenge. Variations in the Mo thickness across the wafer would cause large non-uniformities in T_c. Conversely, the T_c of AlMn-alloy TESs is not controlled by film thickness but rather by the Mn doping concentration in Al and a post-deposition anneal, which we have demonstrated to be reproducible and unaffected by further processing steps [13]. The typical AlMn TES process for AdvACT is a 400 nm deposition of 2000 ppm Mn in Al (at.%), which is patterned, etched, and then annealed at $\sim$235 °C for 10 min. We have achieved T_c uniformity of $\sim$1 % across a 150 mm wafer.

3.3 Dielectric Loss

Low stress, low loss, and high uniformity are important properties of dielectric films used for the types of relieved polarimeter devices being deployed for AdvACT. Dielectric loss in low-temperature superconducting components, such as microstrip transmission lines and integrated filters, can lower the overall coupling efficiency of these detectors to the CMB [17].

In order to characterize the dielectric loss of various materials, we fabricated Nb-dielectric-Nb microstrip resonators in the range of 6–9 GHz and compared their temperature dependence to a model of parasitic two-level-system (TLS) fluctuators [18]. Previously, a recipe for SiO_x was optimized to have low dielectric loss and was used as the dielectric material in ACTPol. Comparing measured TLS loss tangents, we found that the loss tangent of SiN_x (7.8×10^{-4}) was more than a factor of 2 lower than for SiO_x (2.0×10^{-3}). Assuming unchanged loss tangents at the 150/230 GHz frequencies [18], full-circuit post-OMT Sonnet simulations of the microwave components result in a projected 10 % increase in overall detection efficiency by switching to the optimized SiN_x dielectric film. This low-loss SiN_x dielectric also has low stress and uniform composition and thickness across 150 mm wafers.

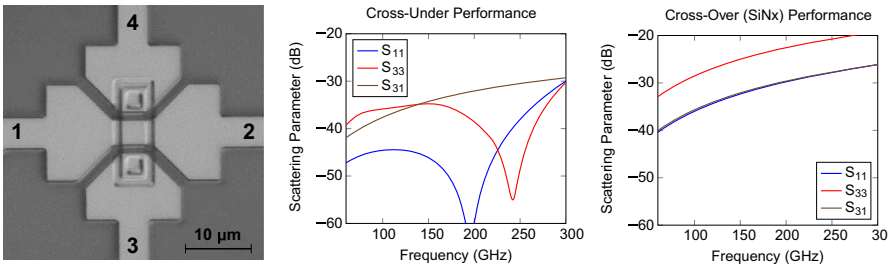

Fig. 3 *Left* Optical microscope image of microwave cross-under showing tapered microstrip to allow for optimized distribution of capacitance, reducing crosstalk and reflections. *Middle* Simulated scattering parameters for the optimized microwave cross-under showing reflections are below −30 dB across the entire frequency range of interest. *Right* Simulated scattering parameters for the microwave cross-over showing reflections are higher than for microwave cross-under across the entire frequency range of interest (Color figure online)

3.4 Microwave Performance

In an effort both to simplify the fabrication process and improve the microwave performance of the detectors, we have implemented a microwave cross-under structure (Fig. 3) which eliminates the need for a third wiring layer, as used in ACTPol. This optimized structure utilizes a 15-μm-wide microstrip section to add extra capacitance to balance the added inductance. Tapering this section allows the extra capacitance to be located as close as possible to the center, which acts to reduce the maximum reflection. Finally, a thin 4-μm-wide microstrip in the center crossing region minimizes crosstalk. A similar geometry has been explored for a microwave cross-over in a three-layer process [19]. Microwave reflection and transmission were simulated via Sonnet (Fig. 3) and show that the cross-under has lower reflections than the cross-over for the entire frequency range of interest.

4 Prototype Multichroic Pixels

Prototyping of the AdvACT polarimeters has included the production of individual pixels on 76.2 mm wafers. These devices match the final pixel design and allow for its appraisal. Feedhorn-coupled optical testing of this design has shown that these polarimeters exhibit well-formed single-moded beams, good optical efficiency, and excellent multichroic passband distinction that is well matched to simulation. Figure 4 shows the passband measurements of three pixels from different radii of two independently fabricated wafers. The pixels show highly uniform response with the largest differences ($\sim$1 % in frequency) being due to a 10 nm difference in dielectric thickness between the two wafers tested. Uniformity tests of dielectric deposition on 150 mm wafers suggest that the vast majority of pixels will have the same dielectric thickness to within $\leq$10 nm.

Various TES-only prototype devices were also fabricated in order to tune and optimize TES characteristics including the superconducting transition temperature, transition shape, normal resistance, and time constant [13]. Noise properties of a TES

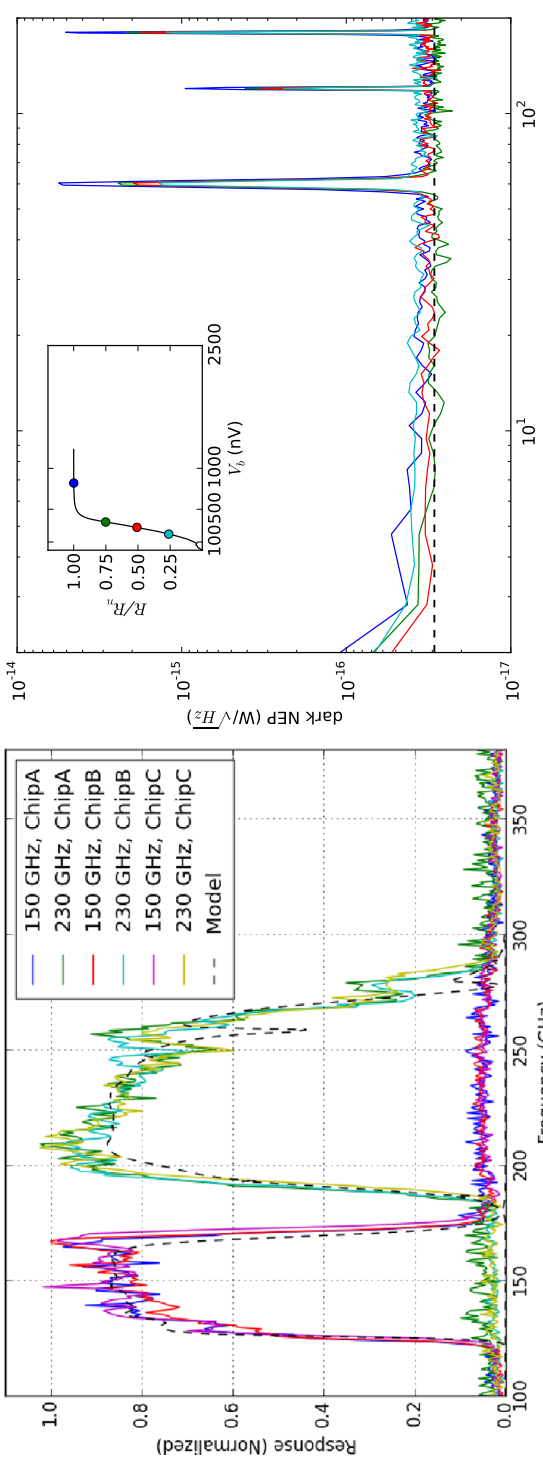

Fig. 4 *Left* Averaged passband measurements of individual multichroic pixel showing the consistency between *x*- and *y*-polarization channels. The data have been normalized to a model of the expected response (*dashed*) developed from simulations of the on-chip filters, OMT, and free space filters used in the measurement. *Right* Noise equivalent power (NEP) for an AlMn TES under no optical loading and at various depths in the transition (*inset*). The white noise level in the science band ($\lesssim$200 Hz) matches that expected from phonon noise (*dashed*). The measured current noise is converted to NEP by using the low frequency responsivity. The low frequency *1/f* noise is not representative of device noise in the field, as this measurement was not optimized for stability at low frequencies. The peaks at 60 Hz and its harmonics represent electrical pickup from AC electronics unique to our lab measurement setup and are not indicative of performance of the devices in the field (Color figure online)

device matching the design to be used in AdvACT (under no optical loading) are shown in Fig. 4. The white noise level at the frequencies relevant to science observations matches that predicted for a phonon noise-dominated device. Such a device will have background limited performance when coupled to the photon loading expected for AdvACT.

5 Conclusions

We have implemented fabrication process improvements for feedhorn-coupled multichroic polarimeter arrays for AdvACT, for a more robust, streamlined, and higher performing detector array as we scale to 150-mm diameter wafers. Fully stepped lithography, a simplified fabrication process, and optimized deposition and etch steps allow for high yields of the densely packed detectors. Replacement of SiO_x with SiN_x is expected to increase the overall detection efficiency by 10 % and switching to AlMn TESs avoids the challenges of MoCu bilayers and provides two ways of tuning the T_c. We have demonstrated multichroic single pixels at 150/230 GHz that exhibit well-formed single-moded beams, good optical efficiency, and multichroic passband distinction that is well matched to simulation.

Acknowledgments This work was supported by the U.S. National Science Foundation through award 1440226. The NIST authors would like to acknowledge the support of the NIST Quantum Initiative. The development of multichroic detectors and lenses was supported by NASA grants NNX13AE56G and NNX14AB58G. The work of BJK, BLS, JTW, and SMS was supported by NASA Space Technology Research Fellowship awards.

References

1. U. Seljak, M. Zaldarriaga, Phys. Rev. Lett. **78**(11), 2054 (1997). doi:10.1103/PhysRevLett.78.2054
2. K.N. Abazajian et al., Astropart. Phys. **63**, 66 (2015). doi:10.1016/j.astropartphys.2014.05.014
3. P.A.R. Ade et al., Phys. Rev. Lett. **112**(24), 241101 (2014). doi:10.1103/PhysRevLett.112.241101
4. D. Hanson et al., Phys. Rev. Lett. **111**(14), 141301 (2013). doi:10.1103/PhysRevLett.111.141301
5. P.A.R. Ade et al., Astrophys. J. **794**(2), 171 (2014). doi:10.1088/0004-637X/794/2/171
6. A. van Engelen et al., Astrophys. J. **808**(1), 7 (2015). doi:10.1088/0004-637X/808/1/7
7. R. Datta et al., J. Low Temp. Phys. **176**, 5–6, 670 (2014), ISSN 0022-2291. doi:10.1007/s10909-014-1134-4
8. J. Hubmayr et al., in *Proceedings of 26th ISSTT* (2015)
9. R. Datta et al., J. Low Temp. Phys., this Special Issue LTD16. doi:10.1007/s10909-016-1553-5
10. S.P. Ho et al., J. Low Temp. Phys., this Special Issue LTD16. doi:10.1007/s10909-016-1573-1
11. S.W. Henderson et al., J. Low Temp. Phys., this Special Issue LTD16. doi:10.1007/s10909-016-1575-z
12. J. McMahon et al., J. Low Temp. Phys. **167**, 5–6, 879 (2012), ISSN 0022-2291. doi:10.1007/s10909-012-0612-9
13. D. Li et al., J. Low Temp. Phys., this Special Issue LTD16 (2015). doi:10.1007/s10909-016-1526-8
14. D.R. Schmidt et al., IEEE Trans. Appl. Supercond. **21**(3), 196 (2011). doi:10.1109/TASC.2010.2090313
15. G.C. ONeil et al., J. Appl. Phys. **107**(9), 093903 (2010). doi:10.1063/1.3369280
16. J.M. Martinis et al., Nucl. Instrum. Meth. Phys. Res. **444**(1–2), 23 (2000). doi:10.1016/S0168-9002(99)01320-0
17. D. Li et al., IEEE Trans. Appl. Supercond. **23**(3), 1501204 (2013). doi:10.1109/TASC.2013.2242951
18. J. Gao et al., in *Proceedings of AIP Conference***1185**, 164–167 (2009). doi:10.1063/1.3292306
19. C.M. Posada et al., Supercond. Sci. Technol. **28**(9), 094002 (2015). doi:10.1088/0953-2048/28/9/094002